Simulation of complex biological flows and flow control problems on Cartesian grids

R. Mittal[1], F.M. Najjar[2], R. Byrganhalli[1], V. Seshadri[1] & H. Singh[3]
[1]*The George Washington University, USA*
[2]*University of Illinois at Urbana-Champaign, USA*
[3]*Thomas Jefferson School of Science and Technology, USA*

Abstract

A recently developed Cartesian grid based immersed boundary method is used to simulate a variety of biological flows as well as flows associated with active flow control. The key feature of the method is that it allows us to simulate flows with complex moving boundaries on stationary Cartesian grids. In this paper we present a brief outline of the method and this is followed by simulation results of a number of flow configurations including human swimming, flapping foils, simulations of flow in a modeled human vocal tract and flow in a synthetic jet flow-control device.

1   Introduction

Recently, there has been a surge of interest in numerical methods that compute flowfields with complex stationary and/or moving immersed boundaries on fixed Cartesian grids [1,2]. Several obvious advantages of these methods over the conventional body-conformal approach are that irrespective of the geometric complexity of the immersed boundaries, the computational mesh remains unchanged. Cartesian grid methods free the underlying structured computational mesh from the task of adapting to the moving boundary, thus allowing large changes in the geometry due to boundary evolution/motion. In the current paper, we apply a recently developed sharp-interface fixed Cartesian grid solver to several configurations with moving boundaries. The simulations include (a) the bio-hydrodynamics of swimming in humans and fish and (b) fluid dynamics of the human vocal tract and (3) simulations of a synthetic jet interacting with a boundary layer.

2   Numerical Method

The schematic in Figure 1 shows a solid body with a curved boundary moving through a fluid, illustrating the current typical flow breadth of problem of interest. The equations solved are the incompressible Navier-Stokes equations, written in tensor form as

$$\frac{\partial u_i}{\partial x_i} = 0, \quad \frac{\partial u_i}{\partial t} + \frac{\partial u_i u_j}{\partial x_j} = -\frac{\partial p}{\partial x_i} + \frac{1}{Re} \frac{\partial^2 u_i}{\partial x_j \partial x_j} \tag{1}$$

where the indices, $i=1,2,3$, represent the x, y and z directions, respectively; while the velocity components are denoted by u (u_1), v (u_2) and w (u_3), respectively. The equations are nondimensionalized with the appropriate length and velocity scales where Re represents the Reynolds number. The Navier-Stokes equations are discretized using a cell-centered, collocated (non-staggered) arrangement of the primitive variables ($\vec{u}$, p). In addition to the cell-center velocities ($\vec{u}$), the face-center velocities, $\vec{U}$, are computed. Similarly to a fully staggered arrangement, only the component normal to the cell-face is calculated and stored. The face-center velocity is used for computing the volume flux from each cell. The advantage of separately computing the face-center velocities has been initially proposed by Zang et al. [3] and discussed in the context of the current method in Ye et al. [2]. The equations are integrated in time using the fractional step method. In the first step, the momentum equations without the pressure gradient terms are first advanced in time. In the second step, the pressure field is computed by solve a Poisson equation. A second-order Adams-Bashforth scheme is employed for the convective terms while the diffusion terms are discretized using an implicit Crank-Nicolson scheme which eliminates the viscous stability constraint. The pressure Poisson equation is solved with a Krylov-based approach.

A multi-dimensional ghost-cell methodology is used to incorporate the effect of the immersed boundary on the flow. The general framework can be considered as Eulerian-Lagrangian, wherein the immersed boundaries are explicitly tracked as surfaces in a Lagrangian mode, while the flow computations are performed on a fixed Eulerian mesh. Hence, we identify cells that are just inside the immersed boundaries as "ghost cells". The discrete equations for these cells are then formulated as to satisfy the imposed boundary condition on the nearby flow boundary to second-order accuracy. These equations are then solved in a fully coupled manner with the governing flow equations of the regular fluid cells. Care has been taken to ensure that the equations for the ghost cells satisfy local and global mass conservation constraints as well as pressure-velocity compatibility relations. The solver has been designed to take geometrical input from conventional CAD program. In the remaining sections, we will demonstrate the application of this method to several flow problems with moving boundaries.

3   Results

Validation studies have been initially performed on canonical flows including the driven cavity, the backward-facing step, flow past a circular cylinder and a sphere. Second-order accuracy has been obtained in space and in time. Comparisons against established experimental and computational results have been undertaken and details have been presented elsewhere [4]. In this section, the solver capabilities are showcased for biological flows including swimming hydrodynamics in humans and fish as well as the fluid dynamics in the human vocal tract. Further, the 3D flow associated with a synthetic jet is also simulated.

3.1. Bio-Hydrodynamics of Swimming Motion

Two different problems in bio-hydrodynamics are being investigated: (1) flow associated with human swimming and (2) the hydrodynamics associated with a fish pectoral fin. The body of the swimmer is scanned and an unstructured grid is used to discretize the surface. 3D simulations are performed on a mesh of 2 million grid points. Figure 2 shows the instantaneous contours of spanwise vorticity past a swimmer at a Reynolds number (based on the body length) of 12,000 for a zero-angle of attack. Flow is observed to closely follow the swimmer body; while flow separation occurs at the aft-end body of the swimmer where small vortices are being shed from the feet. Further studies are being currently performed to substantiate the effects of stroke motion on the flow dynamics. This simulation serves to demonstrate the capability of the flow solver of handling complex geometries

For the study of pectoral fin hydrodynamics 2D simulations have been carried out for a 20% thick elliptic airfoil at a Reynolds number of 300 undergoing a combined pitch and heave motion. The heave amplitude, Strouhal number and pitch amplitude have been fixed at values of 0.5, 0.7 and 40°, respectively. The temporal variations of the pitch angle and the heave are: $\alpha = \alpha_0 + \alpha_1 \sin(2\pi ft + \gamma)$ and $h = h_1 \sin(2\pi ft)$ The wake dynamics is investigated at pitch-bias angles (α_0) varying from 0° to 30°. Contours of the spanwise vorticity field are shown in Figure 3 for the lower and upper bounds of the pitch-bias cases at a phase when the foil is at its center position and moving upwards. For the zero pitch-bias case, a vortex street made up of equal strength clockwise and counter-clockwise vortices is observed. As anticipated this street is oriented along the streamwise direction. For the highest pitch-bias case considered of 30°, substantial modification in the wake topology is observed wherein the small clockwise vortex also gets entrained by the vectored propulsive jet convecting in the direction of the dipole. Change in the pitch-bias angle has a significant effect on the hydrodynamic forces produced by the flapping foil. It was seen that, for a bias-angle greater than about 15°, the foil produces negative thrust or drag. This corroborates with the recent experiments for a rolling-pitching foil [5].

To assess the effects of foil aspect ratio, we consider an elliptical planform foil with major-axes (1.0, 0.2, 2.0) and an aspect ratio, AR=2.55. 3D simulations have been performed for Re= 100 and St=0.5 with a pure heaving motion (no

pitching). Figure 4 presents an isosurface of enstrophy at the time instant corresponding to the lower extreme of the heave cycle. It is observed that the vortex loops and ring-like structures dominate the wake dynamics. Interestingly, these vortex structures are reminiscent of those found in axi-symmetric wakes [6]; and, therefore, the correspondence between the wake topologies of drag and thrust producing *cylinders* extends to 3D bodies. However, the similarity between 2D and 3D flapping foil wakes seems to end there. The dynamics of vortex loops tend to be dominated by the streamwise oriented ``legs'' of the loops which can be modified significantly due to the shear present in the wake. Furthermore, these legs contribute substantially to the streamwise momentum in the wake and are consequently a key determining factor for the thrust of the flapping foil. The diminished importance of spanwise vorticity in the wake of low-aspect ratio flapping foil was well captured in the spanwise vorticity plot on the foil mid-span (not shown). The observed concentrated spanwise vorticity corresponds to the ``heads'' of the vortex loops and these loops are found to be of a relatively lower strength and spaced farther apart from each other than the 2D flapping foil case. Consequently, it is expected that the spanwise vorticity will have a relatively minor contribution to the streamwise wake momentum balance. An extensive computational analysis of these low aspect-ratio flapping foils is currently being conducted and results from this study will be presented in the future.

3.2. Synthetic Jets

The second complex configuration investigated is the synthetic jet which has emerged as a versatile micro-fluidic device in diverse applications ranging from thrust vectoring of jet engines, mixing enhancement to active control of separation and turbulence in boundary layers [7,8,9]. Detailed parametric 2D computations of the synthetic jets have been carried out in the past [10,11]. These studies investigated the effects of variation in the operational parameters like diaphragm amplitude and slot dimensions as well as external flow characteristics. However, from a practical point of view, 3D simulations of the synthetic jets will provide further insight into the flow physics of such devices. The current study focuses on 3D DNS computations to investigate fundamental aspects of synthetic jet flow fields. A schematic of a synthetic jet device is shown in Fig. 5. Typically, such device can be flush mounted on the suction surface of an airfoil. It consists of a piezoelectric membrane mounted onto a metal diaphragm, sealed to form a cavity. The rectangular cavity is defined by width (W), depth (D) and height (H); while a jet slot type is characterized by the width (d), height (h) and depth (w). Fluid is periodically expelled from and entrained into the cavity by the diaphragm oscillation. The oscillation mechanism is described by the deflection amplitude (A) and angular frequency (ω). The external flow is characterized by a freestream velocity (U_∞) and the boundary layer thickness (δ). The jet exit flow evolves in time and space and is characterized by the jet Reynolds number, $Re_d = \overline{V}_j d / v$, and the Stokes number, $S = (\omega d^2 / v)^{1/2}$. Here $\overline{V}_j$ is the average jet exit velocity and $\omega = 2\pi f$, where f is the

forcing frequency. The effects of various *w/d* ratios (1, and 4) keeping the remaining cavity parameters fixed are studied under external quiescent and cross-flow conditions. The grid size consists of 1Million mesh points; while the average jet exit velocity is held fixed at 33.2 with the slot area of 0.46.

Figure 6 shows the isosurface of vorticity, $(\omega^2_x + \omega^2_z)^{1/2}$, under quiescent external flow for the slot shapes considered. It is observed that changes in the slot configuration have large impact on the corresponding outflow as visible from the significant changes in the vortex structures. Thus small changes in the slot configuration lead to large changes in the outflow. It is interesting to notice that the jet emerging out of a rectangular slot gets rotated by 90 deg and aligns itself perpendicular to the slot. Further, it was observed that for square slot, the velocity profile appears 'jet-like' in the maximum expulsion phase is more 'plug-like' during the maximum ingestion phase. The normalized centerline velocity is approximately 2.4 and 2.1 at peak expulsion and ingestion, respectively. With increasing *w/d*, the jet exit profile tends to become more parabolic.

Under the external cross-flow condition, a Blasius flat-plate boundary layer profile is imposed on the jet issuing from the slot lip; while the ratio of *δ/d* was fixed at 2 and $\overline{V}_j / U_\infty$ was held at 0.5. Figure 7 presents the contours of vorticity for two slot types. It is seen that the flow differs significantly from that under quiescent conditions. As the jet interacts with the boundary layer, it is deflected rapidly by 90-deg and evolves parallel to the bottom wall. Ring-like vertical structures are observed to convect in the boundary layer while hair-pin vortices are formed initially. Further, the flow inside the cavity is asymmetric for all the cases due to the imposed external flow. It is observed that in all the cases a shear layer is formed at the jet exit. The computed velocities at the jet exit also show some differences between various cases considered. A general trend observed from all the cases indicates that a shift of the velocity profiles to the right making it unsymmetrical about the center-line of the slot. It is noticed that during the maximum ingestion phase the velocity profiles tends to bulge more as *w/d* increases.

3.3. Fluid Dynamics of the Human Vocal Tract

The third configuration studied is the fluid dynamics of the human vocal tract. The human speed production system has four distinct components; the generator (lungs), the vibrator (larynx), the resonator (pharynx, nasal cavity and sinuses) and articulator (cheek, tongue, teeth, lips). The combined actions of all these components results in distinctive sounds of different classifications namely consonants, vowels, and noises. As an initial step, flow simulations of the air (described as an incompressible flow) have been conducted in a 2D cross-section of the human vocal tract. The considered geometry of the vocal tract corresponds to the generation of a particular vowel. Here, the vibrating motion of the vocal

fold is approximated as a forced movement of the vocal folds undergoing sinusoidal displacement. Contours of spanwise vorticity are plotted in Fig. 8 at four different time instances. The rollup and convection of these vortices are clearly captured. Currently, efforts are being undertaken to incorporate a proper representation of the vocal fold through a multiple mass-spring mode and in future simulations we will also be incorporate vocal tract geometry extracted from MRI scans.

4   Summary

A recently developed numerical method for flows with moving boundaries is used for simulating biological flows in diverse configurations. Its key feature permits to investigate computationally flows with moving boundaries on stationary Cartesian grids with considerably increased computing efficiency over conventional body-conformal structured grid methods. Simulations have been performed of the bio-hydrodynamics of the fish pectoral fin. Further, preliminary numerical study of 3D synthetic jets was performed to gain insight into the flow physics involved with these microjets. It was observed that the presence of cross-flow results in a significantly different flow as evidenced by the dynamics of vortex structures produced by the jet and the jet velocity profiles. The simulations indicate that skewness might be an important characteristic of the jet profile. An initial model of the flow in the human vocal tract was also described.
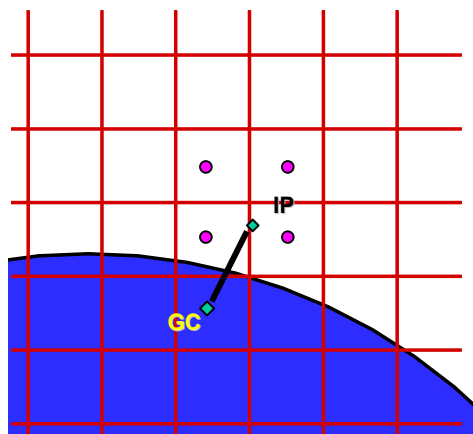
Figure 1. Schematic of the sharp-interface method on a fixed Cartesian mesh, shown are the ghostcell (GC), the image point (IP), and the body boundary.
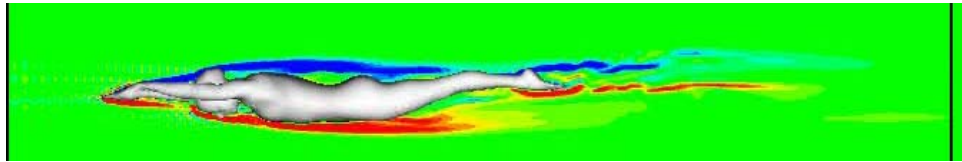
Figure 2. Vorticity contours for the flow past a swimmer, $Re_L = 12,000$.
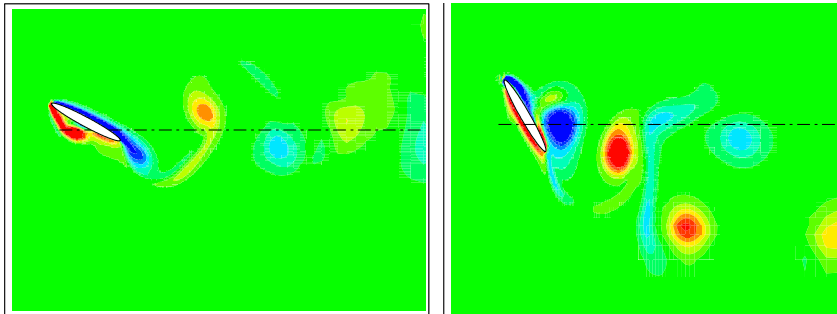

Figure 3. Spanwise vorticity contours for a 2D heaving foil with $\alpha_0=30^o$ at 2 pitch-bias angles (a) $\alpha_1 = 0^o$ and (b) 30°.

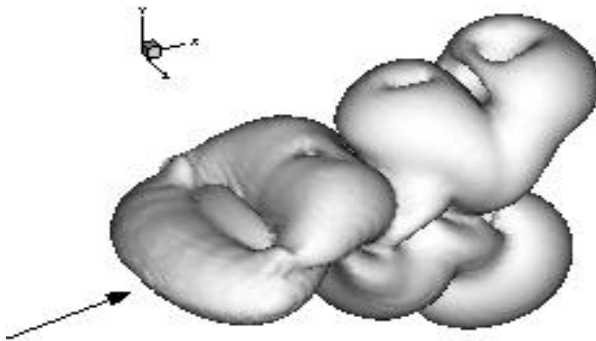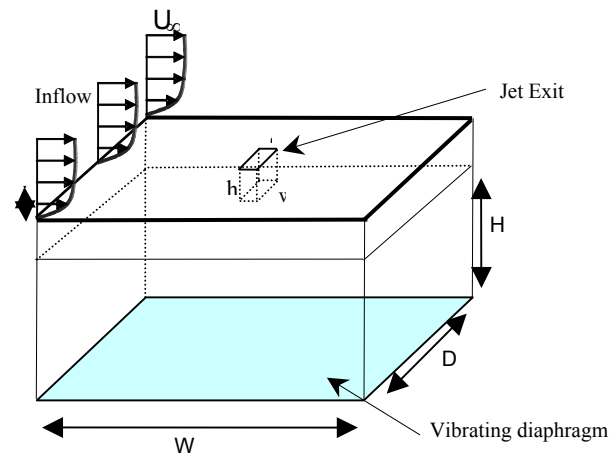Figure 4. Isosurface of enstrophy for a elliptical planform heaving disk.
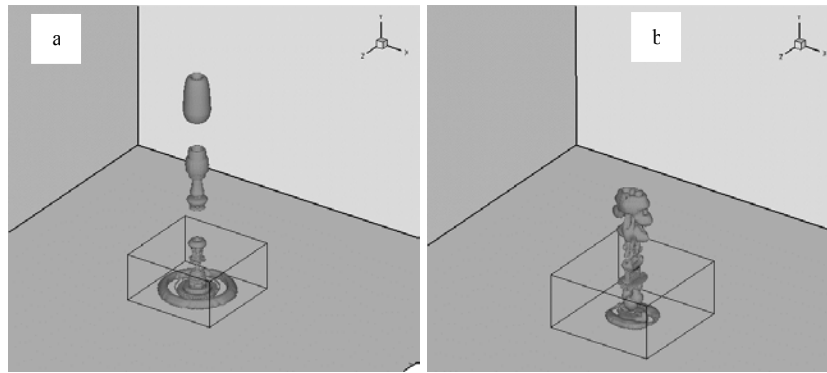
Figure 5. Schematic of a Synthetic Jet

Figure 6. Isosurfaces of vorticity contours in a quiescent flow:
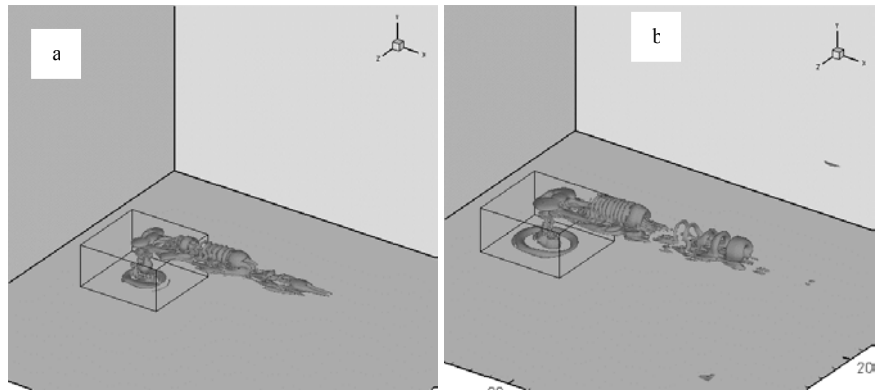(a) *w/d*=1, Re_d=229.3, S=10.8   (b) w/d=4, Re_d=112.84, S=7.58

Figure 7. Isosurfaces of vorticity contours in the presence of an external cross-flow: (a) *w/d*=1 (b) *w/d*=4.
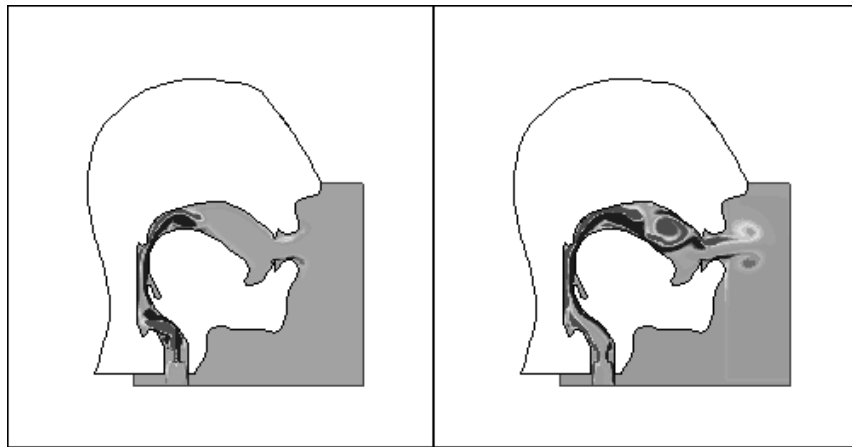

Figure 8. Contours of spanwise vorticity inside the human vocal tract at two time instants.

References

[1] Udaykumar, H. S., Mittal, R., and Shyy, W., "Solid-Liquid Phase Front Computations in the Sharp Interface Limit on Fixed Grids," *J. Comp Phys.,* Vol. 18, pp. 535-574, 1999.

[2] Ye, T., Mittal, R., Udaykumar, H. S. and Shyy, W., "An Accurate Cartesian Grid Method for Viscous Incompressible Flows with Complex Immersed Boundaries," *J. Comp. Phys.* Vol. 156, pp. 209-240, 1999.

[3] Zang, Y. Street R. L. and Koseff, J. R., *"*A non-staggered Grid, Fractional Step Method for Time-Dependent Incompressible Navier-Stokes Equations in Curvilinear Coordinates," *J. Comput. Phys*. 114, 18, 1994.

[4] Najjar, F.M., and Mittal, R., "Simulations of Complex Flows and Fluid-Structure Interaction Problems on Fixed Cartesian Grids," FEDSM 2003-45577, Proceedings of FEDSM'03, 4th ASME-JSME Joint Fluids Engineering Conference, July 6-11, Honolulu, Hawaii, 2003.

[5] Triantafyllou, G.S., Triantafyllou, M.S., and Grosenbaugh, M.A., "Optimal Thrust Development in Oscillating Foils with Applications to Fish Propulsion," *J. Fluids Struc*., Vol. 7, pp. 205-224, 1992.

[6] Mittal, R., Wilson J.J., and Najjar, F.M., "Symmetry Properties of the Transitional Sphere Wake," *AIAA J.*, Vol. 40, No. 3, 2002.

[7] Wygnanski, I., "Boundary Layer and Flow Control by Periodic Addition of Momentum," AIAA 97-2117, 1997.

[8] Chen, Y., Liang, S., Anug, K., Glezer, A., Jagoda, J. (1999), Enhanced mixing in a Simulated Combustor Using Synthetic Jet Actuators*.* AIAA 99-0449.

[9] Davis, S.A., Glezer, A., "Mixing Control of Fuel Jets using Synthetic Jet Technology: Velocity Field Measurement," AIAA 99-0447, 1999.

[10] Mittal, R., Rampunggoon, P. Udaykumar, H.S., "Interaction of a Synthetic Jet with a Flat Plate Boundary Layer," AIAA 2001-2773, 2001.

[11] Utturkar, Y., Holman, R., Mittal, R., Carroll, R., Sheplak, M., and Cattafesta, L., "A Jet Formation Criterion for Synthetic Jet Actuators," AIAA 2003-0636, 2003.